Biochemical Engineering Journal 227 (2026) 110049

Contents lists available at ScienceDirect

Biochemical Engineering Journal

journal homepage: www.elsevier.com/locate/bej

Regular Article

Hybrid section-based modeling of gas-phase hydrodynamics in biotrickling filters: Influence of packing material on residence time distributions

Felipe A. Carreño-López [a,b], Patricio A. Moreno-Casas [a], Felipe Scott [a], Alberto Vergara-Fernández [a], José Sierra-Pallares [c], Raúl Muñoz [b,*]

[a] Green Technologies Research Group (GTech), Facultad de Ingeniería y Ciencias Aplicadas, Universidad de los Andes, Mons. Álvaro del Portillo 12455, Las Condes, 7620001, Santiago, Chile

[b] Institute of Sustainable Processes, Departamento de Ingeniería Química y Tecnología del Medio Ambiente, Universidad de Valladolid, Dr. Mergelina, Valladolid, 47011, Spain

[c] Departamento de Ingeniería Energética y Fluidomecánica & ITAP, Escuela de Ingenierías Industriales, Universidad de Valladolid, Paseo del Cauce 59, Valladolid, Spain

ARTICLE INFO

Dataset link: Data (Original data)

Keywords:
Axial dispersion
Biotrickling filters
Biofiltration
Gas treatment
Residence time distribution

ABSTRACT

In this study, the gas-phase hydrodynamics within a 6.5 L biotrickling filter were quantified using pulse-injection residence time distributions (RTDs) recorded with a cost-effective metal oxide (MOx) sensor. This was conducted at a constant gas flow rate of 8 L min^{-1} across trickling liquid velocities (TLV) ranging from 0 to 10 m h^{-1}, using three different packings: polyurethane foam, Tri-Packs Jaeger spheres, and wood bark. A hybrid section-based model was developed and evaluated against two closed-closed axial dispersion variants (AD$_{cc}$+CSTR and AD$_{cc}$+PFR). Model discrimination using AIC/BIC and R^2 indicated that the optimal model description is contingent upon the packing material and operating regime: the hybrid model most accurately represented foam and most wood cases, whereas AD$_{cc}$+CSTR was sufficient for spheres under irrigation, and AD$_{cc}$+PFR consistently underperformed. Employing the optimal model in each scenario, the Peclet number increased with TLV for PUF and spheres (with diminishing returns at the highest TLV), whereas wood exhibited a low Peclet number and non-monotonic behavior. By explicitly partitioning the mean residence time between the buffer zones and the bed, the hybrid model effectively separates the boundary hold-up from the core dispersion, yielding a more precise representation of the packed bed Peclet number. Overall, MOx-based RTD measurements, in conjunction with model comparison, offer a cost-effective in situ diagnostic tool for differentiating boundary mixing from bed transport, thereby informing packing selection and operating parameters in gas-phase biofiltration.

1. Introduction

Biotechnologies have been increasingly recognized as cost-efficient and environmentally sustainable technologies for the treatment of air streams polluted with low-to-moderate concentrations of volatile organic compounds (VOCs) and inorganic odorants, typically not exceeding 5 g m^{-3} [1]. In particular, biotrickling filtration (BTF) has gained prominence not only because of its cost-effectiveness in VOC and odor control but also because of its applicability in hydrogenotrophic biogas upgrading and biogas desulfurization processes [2,3].

This bioreactor configuration allows long-term operation under a reduced pressure drop with lower operational costs than those of biofilters and bioscrubbers [4]. The configuration of biotrickling filters consists of a tubular packed bed reactor in which the gas and liquid phases flow co-currently or counter-currently over a packing material to transfer pollutants from the gas phase to a microbial community attached to the packed bed. These gaseous pollutants are used as carbon and energy sources by microorganisms, whereas nutrients such as nitrogen, phosphorus, and trace metals are supplied from the recirculating liquid phase [5]. This technology involves a complex combination of physicochemical and biological phenomena, where the mass transfer of pollutants and biodegradation are the main factors that govern the performance of biotrickling filters.

In this context, the transferred species are volatile contaminants found within the bulk gas, whereas the receiving phase is the microbial biofilm attached to a solid support structure. The transfer occurs either directly across a gas–biofilm interface, where the biofilm is exposed to the gas, or indirectly through dissolution into the surrounding liquid, followed by diffusion through the liquid film into the biofilm.

---

[*] Corresponding author.
E-mail address: raul.munoz.torre@uva.es (R. Muñoz).

https://doi.org/10.1016/j.bej.2025.110049
Received 15 July 2025; Received in revised form 12 December 2025; Accepted 12 December 2025

Consequently, the overall resistance includes the gas-side boundary layer, interfacial transfer (gas–liquid), liquid-side boundary layer, and diffusion within the biofilm, where biodegradation occurs [6]. Thus, the choice of packing material is fundamental for facilitating biofilm growth and sustaining an effective gas-liquid interface for gas pollutant abatement [5,7].

Several materials, ranging from organic materials such as compost, wood chips, and coconut fiber to inert supports such as perlite, plastic rings, and polyurethane foam, have been used to balance biological compatibility with structural stability [8]. To date, the selection criteria have typically prioritized a large specific surface area (ideally $\geq 600\,\mathrm{m}^2\,\mathrm{m}^{-3}$), high porosity, nutrient content, moisture retention, slow biodegradability, minimal pressure drop, and cost effectiveness [9]. Most studies have focused on the physical properties rather than the hydrodynamics of the packing materials. Therefore, there is a knowledge gap regarding the influence of the structure of packing materials on BTF hydrodynamics, which is a promising research field for improving the pollutant-abatement performance of these technologies [10].

The hydrodynamics of biotrickling filters are primarily determined by the superficial trickling liquid velocity (TLV) within the packed bed, which refers to the liquid flow rate per unit column cross-sectional area. Empirical studies have demonstrated that variations in this velocity have a more significant impact on BTF performance than do changes in the gas flow rate [11]. In biotrickling filters, the superficial trickling liquid velocity is typically maintained below $10\mathrm{mh}^{-1}$ [12]. Increasing this velocity can improve the wetted surface area of the packing, which may enhance biofilm development and promote gas–liquid mass transfer [13,14]. However, excessive velocities can increase liquid holdup and shear forces, potentially detaching the biofilm and reducing overall reactor performance.

Studies comparing structured and random cubic polyurethane foams as packing material configurations have yielded significantly different results [15,16]. This divergence in the findings was explained by the influence of the liquid flow velocity, which was identified as a key variable in the experimental design. This provided relevant conclusions regarding the influence of packing material on process performance, highlighting the critical influence of TLV on the effectiveness of the packing material in different setups. However, a recent study demonstrated that the implementation of intermittent trickling regimes can enhance the performance of biotrickling filters used for biogas upgrading, with the improvement attributed to substantial substrate conversion occurring in the non-wetted regions of the biofilm [17]. This suggests that gas-phase transport, particularly in partially saturated systems, is critical to the overall reactor efficiency. These findings highlight the need for further investigation of gas flow dynamics in BTFs, especially under low residence time conditions, where gas–biofilm contact may dominate the mass transfer. Accordingly, understanding gas-phase dispersion is essential for elucidating the interactions between the gas and liquid phases and evaluating the influence of packing material on pollutant removal performance.

The analysis of the residence time distribution (RTD) can play a key role in identifying flow anomalies, which is a fundamental aspect of understanding the dynamics of fluid flow in BTFs [18,19]. This method is particularly effective for identifying dead zones and short-circuiting within BTFs and can contribute to reducing the overall size and operational costs of biofiltration systems [20]. Previous studies have used this technique to assess the hydrodynamic characteristics of BTFs based on the liquid phase [21–23]. However, the liquid-phase RTD cannot be used to analyze preferential flows and maldistribution in the gas phase. The accurate determination of the gas-phase RTD in BTFs necessitates the real-time monitoring of gas-phase tracers [24]. Unfortunately, RTD tests over the gas phase in biofilter reactors are scarce [25]. This is attributed to the fact that conventional analytical and instrumental methodologies for determining tracer gas concentrations cannot provide instantaneous measurements (e.g., gas chromatography and flow injection analysis systems). Tracer absorption in the liquid phase interferes with the determination of the tracer RTD, and techniques such as time-of-flight mass spectrometry are expensive and unavailable in most laboratories. However, the underlying principles and operational methodologies of e-nose instruments suggest their potential application in the accurate determination of RTD in gas treatment reactors [26]. In a recent study, an RTD analysis of the gas phase in a conventional biofilter was effectively conducted using a low-cost MOx sensor, underscoring its potential utility in BTFs [18].

Building upon this methodology, the current study employed a series of pulse-based RTD experiments to examine the gas-phase hydrodynamics in a laboratory-scale BTF equipped with an MOx sensor. This study specifically assessed the impact of three distinct packing materials—polyurethane foam, Jaeger Tri-Packs spheres, and wood bark— on a wide range of trickling liquid velocities (TLVs). To complement the experimental findings, a hybrid RTD model that explicitly accounts for residence time contributions from nonreactive buffer zones was proposed and benchmarked against two classical axial-dispersion formulations: one with closed–closed Danckwerts boundaries coupled to two CSTRs (representing the buffer zones) and the other with the same axial-dispersion core bounded by two plug-flow segments. By elucidating the interactions between the gas and liquid at varying TLVs and their influence on dispersion behavior, this approach aims to enhance the understanding of gas phase dynamics in BTF systems. The integration of low-cost sensing with numerical modeling provides a scalable and practical framework that can contribute to the cost-effective design and optimization of gas-phase biofiltration systems in the future.

2. Materials and methods

2.1. Experimental setup

As shown in Fig. 1, the experimental setup comprised a transparent PVC tubular reactor with a 6.5 L capacity. This included a cylindrical unit measuring 0.566 m in height and 0.115 m in internal diameter connected to a lower conical funnel with a height of 0.08 m. The air inlet and outlet pipelines were positioned 0.15 and 0.58 m, respectively, from the base of the cylindrical units. The packing material was placed 0.01 m above the gas inlet, with a total height of 0.4 m.

The gas tracer injection port consisted of a glass tube Afora™V83120 (Afora S. A., Spain) equipped with a butyl septum, positioned 0.06 m before the column inlet. Inlet and outlet polyamide pipelines, each with an internal diameter of 8 mm, delivered the gas and liquid phases directly into and out of the reactor, respectively. The gas flow rate was regulated using a rotameter (Aalborg), and a peristaltic pump (520-S, Watson Marlow, UK) circulated distilled water from a magnetically stirred 2.2 L external water tank through the packed bed of the column. In this study, trickling water was directly pumped into the column without the incorporation of a spray unit.

2.2. Packing materials

Three different packing materials were investigated in this study: wood bark with a porosity of 0.530 [27]; polyurethane foam (PUF) (Filtren ™25280, Recticel Iberica S.L., Spain) with a density of $10\,\mathrm{kg\,m}^{-3}$, a specific surface area of $1000\,\mathrm{m}^2\,\mathrm{m}^{-3}$, a porosity of 96%, and a water retention capacity of $0.12\,\mathrm{L}_{\mathrm{water}}\mathrm{L}_{\mathrm{PUF}}^{-1}$; and Jaeger Tri-Packs® Spheres (Raschig Jaeger Technologies, Ludwigshafen, Germany), hereafter referred to simply as spheres, with a density of $67.3\,\mathrm{kg\,m}^{-3}$, specific surface area of $157\,\mathrm{m}^2\,\mathrm{m}^{-3}$ and a porosity of 93.5%. These packing materials were positioned 0.01 m above the gas inlet and filled up to 0.40 m from the bottom of the cylindrical unit, accounting for a total volume of 4.2 L.

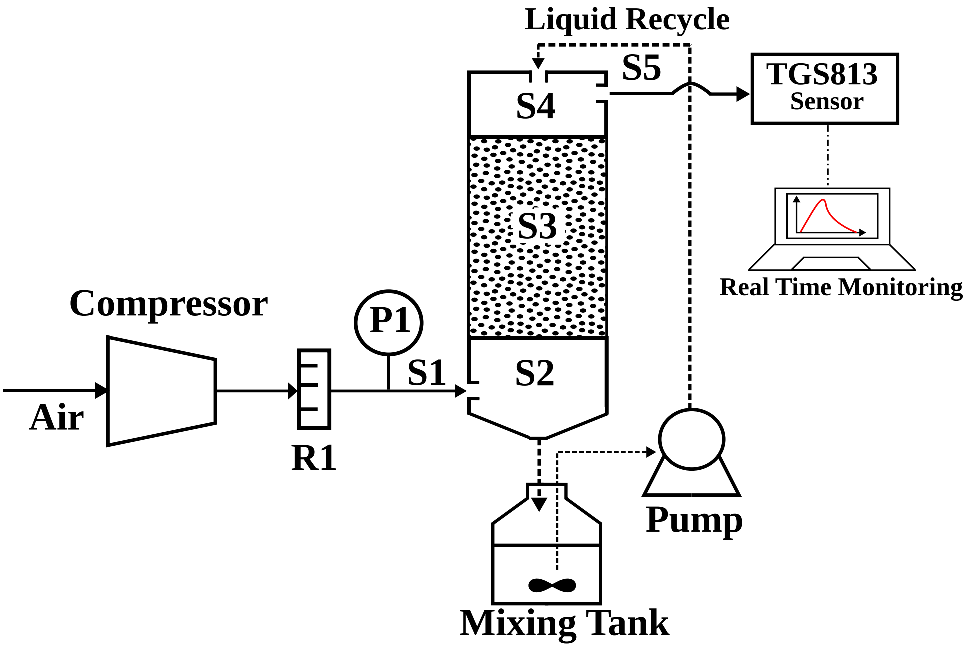

Fig. 1. Schematic of the packed bed reactor used for RTD tests. The vessel was partitioned into five zones for modeling: S1, the inlet line, S2 the lower buffer section, S3 the packed-bed section, S4 the upper buffer section; and S5, the outlet line. The gas tracer is injected upstream of S1 and detected at the outlet of S5.

2.3. Experimental procedure

Butane (Butsir, Barcelona, Spain) was selected as the gas tracer because of its stability, non-biodegradability, low water solubility, and ease of handling. A FIGARO TGS813 series sensor (RS Components, Madrid, Spain) was used to conduct the gas tracer experiments. This sensor employs tin dioxide as its sensing material and operates effectively within a detection range of 500–10 000 ppmv for gas concentrations in air. It is highly sensitive to various reducing gases and was selected for this study because of its cost-effectiveness and ease of integration into the sensor system. The sensor was mounted on an Arduino Uno board and interfaced with a 16-bit analog-to-digital converter (ADC). This setup was connected via USB to a standard laptop or desktop computer for data acquisition and control using an open-source software developed in Python 3.7. The TGS813 sensor functions as a simple voltage divider circuit. The sensor resistance (R_s) was calculated using the following equation:

$$R_s = \left(\frac{V_{cc}}{V_{RL}} - 1\right) \cdot R_L \tag{1}$$

In this equation, R_L represents the load resistance, V_{cc} is the supply voltage applied across the sensor, and V_{RL} is the voltage measured across R_L, which reflects the sensor response. In this study, V_{cc} and R_L were set to 5 V and 10 kΩ, respectively. The initial voltage and saturation voltage of the sensor were 0 and 2.88 V, respectively. The mathematical model introduced by Monroy et al. [28] was used in this study to filter the sensor recovery time. This model categorizes the sensor into three distinct stages: measurement circuit, transient behavior, and transduction stage. Initially, the transient resistance is derived from Eq. (1) during the measurement circuit stage, respectively. Subsequently, the steady-state resistance was retrieved during the transient behavior stage using Eq. (2):

$$R_1(t) \propto R_2(t) + \tau_i \frac{R_2(t) - R_2(t-1)}{\Delta t} \tag{2}$$

Here, Δt represents the data acquisition rate, τ_i is the time constant of either the rising phase τ_r or the recovery phase τ_d, and $R_1(t)$ and $R_2(t)$ denote the resistances in the steady state and transient behavior at time step t, respectively. This study disregards the filtering of the transient signal response, which refers to the initial rapid change in the sensor output during tracer breakthrough based on the recovery time constant. This decision was based on the finding that the gas flow promoted signal recovery at a rate of 0.622 s^{-1}, which is consistent with the value reported for the same gas flow, resulting in rapid recovery times. [18].

Subsequently, the raw voltage data were post-processed to a normalized resistance value ($\frac{R_s}{R_0}$) to estimate the tracer concentration using the technical information provided by the manufacturer. The parameter R_0 denotes the sensor resistance at 1000 ppmv of methane under atmospheric conditions. According to the manufacturer's calibration protocol, this reference value must be used to correctly derive gas concentrations from the sensor response. This value was obtained by measuring the sensor resistance inside a plastic container adapted to allow the sensor to hang in the middle of the container and injecting 70 μL of pure methane with a 500 μL gas-tight Hamilton syringe to achieve concentrations near 1000 ppmv inside the container. In the final step, the resistance R_0 was determined using Eq. (1) and subsequently employed to calculate the tracer concentration values by applying the manufacturer's sensitivity data using Eq. (3):

$$C = 10^{-2.1116 \cdot \log\left(\frac{R_s}{R_0}\right) + 2.7412} \tag{3}$$

Here, the values −2.116 and 2.7412 were derived empirically from the calibration curve supplied by the manufacturer. Prior to conducting the experiments, the MOx sensor was preheated by connecting it to the current and maintaining it in an energized state for 12 h, as recommended by the manufacturer, to ensure stable performance. The experiments were carried out under controlled ambient conditions (typically $T \approx 298.15$ K, $p \approx 1$ bar, RH $\approx$ 60%). To account for the effects of temperature and humidity, as well as sensor drift, a new calibration curve was established at the beginning of each experimental day under prevailing conditions. The inlet airflow was adjusted to 8 $\text{L}\,\text{min}^{-1}$, which corresponded to an empty bed residence time of 48.9 s. The average velocity within the inlet tube, calculated to be 2.65 $\text{m}\,\text{s}^{-1}$, was derived from the relationship between the volumetric flow rate and the cross-sectional area in the flow direction. This resulted in a laminar flow regime, as indicated by a Reynolds number of 1310.58, which was below the threshold of 2300. The corresponding ideal space–time values were obtained by dividing the reactor volume by the volumetric gas flow rate and correcting for the porosity of each packing material, as detailed in the following sections. Based on the measured porosities, the resulting ideal space times were 46.94, 45.72, and 26.90s for the PUF, spheres, and wood bark, respectively. Distilled water was pumped from an external holding tank at rates of 0, 2, 5, and 10 $\mathrm{m\,h^{-1}}$. Each assay commenced with a 15-minute stabilization period to establish equilibrium in air and liquid flow, equating to approximately 900 s (i.e., approximately 18.4 times the ideal space time). Typically, a steady state is achieved within 3–4 space times [29]. Subsequently, a 10 mL butane pulse was injected manually in less than one second using a 20 mL polypropylene gas-tight syringe. The injection procedure mimicked a Dirac delta function (very short-duration high-intensity tracer input) and ensured minimal yet detectable tracer presence (less than 1% of the gas volume inside the reactor). The MOx sensor was configured to acquire data at a rate of 20 Hz, with a total graphing duration of 200 s per injection. This duration was approximately four times the theoretical residence time, ensuring comprehensive capture of the tail of the RTD curve. After each experiment, a 10-minute clean airflow period was introduced to prepare the reactor for subsequent runs.

2.4. *Experimental residence time distribution*

Tracer elements follow various paths through the reactor, resulting in different residence times for each pathway. The RTD characterizes the time required for a gas stream to exit a reactor. This distribution, also referred to as the exit age distribution $E(t)$, describes the probability density of the fluid elements leaving the vessel. This is mathematically defined by Eq. (4):

$$E(t) = \frac{C(t)}{\int_0^\infty C(t)\,dt} \tag{4}$$

where $C(t)$ is the tracer concentration monitored at the reactor outlet over time t. The mean residence time (t_m) describes the first moment and is calculated as follows:

$$t_m = \int_0^\infty t\,E(t)\,dt \tag{5}$$

In packed bed reactors, this value helps detect dead zones and bypasses by comparing it with the theoretical residence time $\bar{\tau}$:

$$\bar{\tau} = \frac{\varepsilon V_r}{Q} \tag{6}$$

where ε is the packing material porosity, V_r denotes the reactor volume ($\mathrm{m^3}$), and Q is the volumetric gas flow ($\mathrm{m^3\ s^{-1}}$). Fluid bypassing certain regions within the system can occur when t_m exceeds $\bar{\tau}$. Conversely, if t_m is lower than $\bar{\tau}$, stagnant zones in which the fluid may be trapped or remain immobile may form. By analyzing the discrepancies between t_m (the experimentally determined average residence time) and $\bar{\tau}$ (the theoretical average residence time), the hydrodynamic efficiency of the reactor can be assessed, and issues such as insufficient mixing and fluid bypass can be identified. This understanding will improve the design and operation of BTFs in the future. In biofiltration, porosity is often neglected, and the empty bed residence time (EBRT) is typically used to describe gas retention. In this study, however, the EBRT was calculated theoretically based on the reactor volume and gas flow rate. It is important to note that EBRT tends to overestimate the duration for which gas remains in BTFs. The second moment (σ^2) quantifies the deviations from plug flow. This parameter is essential for assessing the degree of flow non-ideality, such as channeling, dispersion, or dead zones, which can significantly impact reactor performance. It was calculated using Eq. (7):

$$\sigma^2 = \int_0^\infty (t - t_m)^2 E(t)\,dt \tag{7}$$

The estimated σ^2 and t_m were subsequently used to determine the parameter bounds and initial values for the model fitting process.

3. Residence time distribution modeling

In this study, a hybrid section-based RTD model was proposed and evaluated against two closed-closed axial dispersion formulations. The hybrid model conceptualizes the column as composed of five zones in series: the inlet line, lower buffer zone, packed bed, upper buffer zone, and outlet line. In this configuration, the buffer zones were modeled as continuous stirred-tank reactors (CSTRs), the packed bed was characterized by the axial-dispersion kernel, and the inlet/outlet lines were treated as pure delays with a constant residence time of 0.023s, based on their short length and the absence of significant mixing or recirculation in these zones. This hybrid model was compared with an axial dispersion model featuring closed–closed Danckwerts boundaries coupled with two CSTRs, one for each buffer zone (Model A: CSTR→AD_{cc}→CSTR), and the same axial dispersion model bounded by two plug flow zones, one for each buffer zone (Model B: PFR→AD_{cc}→PFR). For consistent reporting across models, the characteristic times associated with the two buffer regions are denoted by t_{B1} and t_{B2} (s), the mean residence time of the dispersed bed by t_{PBR} (s), and the overall mean by t_m (s). Thus, t_{B1} refers to the lower buffer region (entry) and t_{B2} refers to the upper buffer region (exit). Three alternatives were formulated to enforce mass conservation and normalized age densities, which were subsequently calibrated and compared using the same experimental residence time distribution (RTD) data.

3.1. *Axial–dispersion model*

Gas–phase nonidealities in the packed bed were described using the one–dimensional convection–dispersion equation written in terms of the Peclet number:

$$\mathrm{Pe} = \frac{uL}{D_{\mathrm{ax}}}, \qquad t_{\mathrm{PBR}} = \frac{L}{u},$$

Let $x = z/L \in (0,1)$ and t, the governing equation becomes

$$\frac{\partial c}{\partial t} = \frac{1}{\mathrm{Pe}\,t_{\mathrm{PBR}}}\frac{\partial^2 c}{\partial x^2} - \frac{1}{t_{\mathrm{PBR}}}\frac{\partial c}{\partial x}, \qquad 0 < x < 1,\ t > 0, \tag{8}$$

with the initial condition $c(x,0) = 0$. The closed–closed (Danckwerts–type) boundary conditions are expressed in the unified Robin form [30]:

$$\begin{aligned} &\text{at } x = 0: \quad c(0^+,t) - \frac{1}{\mathrm{Pe}}\left.\frac{\partial c}{\partial x}\right|_{0^+} = c_{\mathrm{in}}(t), \\ &\text{at } x = 1: \quad c(1^-,t) + \frac{1}{\mathrm{Pe}}\left.\frac{\partial c}{\partial x}\right|_{1^-} = c_{\mathrm{out}}(t) \end{aligned} \tag{9}$$

where $c_{\mathrm{in}}(t)$ and $c_{\mathrm{out}}(t)$ depend on the external elements attached to the bed,

3.2. *Model A: CSTR → AD_{cc} → CSTR*

Two buffer zones modeled as CSTRs, with residence times t_{B1} and t_{B2}, are positioned before and after the packed bed, which has a mean time t_{PBR}. For a unit pulse at the model entry point, the buffer concentrations are governed by:

$$t_{B1}\frac{dc_{B1}}{dt} + c_{B1} = \delta(t), \qquad c_{B1}(0) = 0,$$

$$t_{B2}\frac{dc_{B2}}{dt} + c_{B2} = c(L,t), \qquad c_{B2}(0) = 0$$

In the unified Danckwerts formulation [30], the connection between the bed inlet and outlet is expressed as:

$$c_{\mathrm{in}}(t) = c_{B1}(t), \qquad c_{\mathrm{out}}(t) = c_{B2}(t)$$

Consequently, the observed exitage density is directly linked as follows:

$$E_{\mathrm{out}}(t) = c_{B2}(t) \tag{10}$$

3.3. Model B: PFR → AD_{cc} → PFR

In this scenario, the buffer zones function as plug–flow delays with durations of t_{B1} at the inlet and t_{B2} at the outlet, whereas the bed has a duration of t_{PBR}. In its unified form, this is expressed as

$$c_{\text{in}}(t) = \delta\big(t - t_{B1}\big), \qquad c_{\text{out}}(t) = c(L,t) \tag{11}$$

This configuration simplified the right boundary to a zero–gradient condition, $c_z(L^-, t) = 0$. Consequently, the exit–age density is equivalent to the bed impulse response adjusted by the total delay, as follows:

$$E_{\text{out}}(t) = c\big(L,\, t - t_\ell\big)\ H\big(t - t_\ell\big), \qquad t_\ell = t_{B1} + t_{B2} \tag{12}$$

The Heaviside step function $H(t)$ and Dirac delta function $\delta(t)$ were employed to represent the step and impulse inputs, respectively, in the formulation of the boundary conditions and the age–density functions.

3.4. Model C: Hybrid section–based model

The buffer sections are described below.

$$E_{\text{CSTR}_i}(t) = \frac{1}{t_{Bi}} \exp\left(-\frac{t}{t_{Bi}}\right) H(t), \quad i = 1,2 \tag{13}$$

whose series combination yields

$$E_{12}(t) = \begin{cases} \dfrac{e^{-t/t_{B2}} - e^{-t/t_{B1}}}{t_{B2} - t_{B1}}\ H(t), & t_{B1} \neq t_{B2} \\ \dfrac{t}{t_B^2}\ e^{-t/t_B}\ H(t), & t_{B1} = t_{B2} = t_B \end{cases} \tag{14}$$

The packed–bed kernel used in the hybrid structure was an open–open impulse response:

$$E_{\text{PBR}}(t) = \frac{u}{\sqrt{4\pi D_{\text{ax}}\, t}} \exp\left[-\frac{(L - ut)^2}{4D_{\text{ax}}\, t}\right] H(t), \tag{15}$$

Finally, the outlet age density is expressed as

$$E_{\text{out}}(t) = \int_0^{t-t_\ell} E_{12}(\xi)\, E_{\text{PBR}}\big(t - t_\ell - \xi\big)\, d\xi\ H(t - t_\ell), \qquad t_\ell = t_{\text{in}} + t_{\text{out}} \tag{16}$$

All age densities satisfied $\int_0^\infty E(t)\,\mathrm{d}t = 1$.

3.5. Model selection and comparison

Each candidate model was fitted to the experimental RTD data to enable fair selection and comparison by adjusting the parameters t_{B1}, t_{B2}, t_{PBR}, and Pe. The initial guesses were 11.02 s, 6.72 s, 31.16 s, and 12, respectively. These values correspond to the empty bed residence times, which were directly calculated from the gas flow rate and volume of each section. To ensure physically meaningful results, the parameters were constrained within the bounds of 0 to 30 s for t_{B1}, t_{B2}, and t_{PBR}, and 0 to 30 for Pe, to reflect physically plausible residence times based on reactor geometry and flow rates, and to ensure numerical stability during the model fitting. The selected Pe range and starting value were determined to capture the expected level of axial dispersion typically observed in packed beds under these flow conditions. The optimization minimized the sum of the squared residuals (see equation below) between the experimental RTD, $E_{\text{exp}}(t)$, and the modeled RTD, $E_{\text{model}}(t)$:

$$\text{Residual} = \sum_i \big(E_{\text{exp}}(t_i) - E_{\text{model}}(t_i)\big)^2 \tag{17}$$

The optimization used a convergence tolerance of 10^{-8} on parameter updates, with a hard cap of 4000 objectivefunction evaluations (`max_nfev` = 4000). Finally, the Akaike and Bayesian information criteria were used to select the mathematical model that best estimated the experimental data [31].

3.6. Internal validation and uncertainty quantification

The reliability of the estimated hydrodynamic parameters and the uncertainty linked to model calibration were assessed using an internal validation method that employed a residual nonparametric bootstrap. Bootstrap techniques have been widely used in chemical and biochemical engineering to quantify uncertainties in nonlinear parameter estimation and reactor modeling. [32–35].

Subsequent to the calibration of each model to the experimental RTD, the residuals were determined as follows:

$$r_i = E_{\text{exp}}(t_i) - E_{\text{model}}(t_i). \tag{18}$$

For each packing material, TLV condition, and model (AD_{cc}+CSTR, AD_{cc}+PFR, hybrid), $B = 200$ residual–bootstrap replicates were generated. Resampling was performed with NumPy's `default_rng` using a fixed seed (12 345) to ensure exact reproducibility, and insensitivity to alternative seeds was verified. In each replicate, the residuals were sampled with replacement and added to the model prediction:

$$E^{*(b)}(t_i) = E_{\text{model}}(t_i) + r_i^{*(b)}, \qquad b = 1, \dots, B. \tag{19}$$

This method adheres to the suggested guidelines for handling uncertainty propagation in nonlinear models within process systems engineering [35,36].

Each bootstrap dataset $E^{*(b)}(t)$ was refitted using the same optimization scheme described in Section 3.5. In this manner, bootstrap distributions were obtained for all estimated parameters. Empirical 95% confidence intervals (CI_{95}) were determined using the 2.5th and 97.5th percentiles of the respective bootstrap distributions [33,37].

To evaluate the statistical calibration of each model, the coverage of the asymptotic 95% confidence intervals, which were derived from the covariance matrix of the nonlinear regression, was determined. For parameter θ, coverage is defined as follows:

$$\hat{C}(\theta) = \frac{1}{B} \sum_{b=1}^{B} \mathbb{I}\big[\hat{\theta} - z_{0.975}\,\text{SE} \ \le\ \theta^{*(b)} \ \le\ \hat{\theta} + z_{0.975}\,\text{SE}\big] \tag{20}$$

In this context, $\hat{C}(\theta)$ represents the empirical coverage and B indicates the total number of bootstrap replicates. The estimate derived from the bth bootstrap sample is denoted as $\theta^{*(b)}$. The asymptotic estimate and standard error from the initial fit are represented by $\hat{\theta}$ and SE, respectively. The value $z_{0.975} = 1.96$ specifies the 95% confidence limits, and $\mathbb{I}[\cdot]$ serves as an indicator function. This bootstrap method facilitated the incorporation of calibration uncertainties into all the hydrodynamic descriptors. Analyses were performed in Python 3.13.9 using the `lmfit` nonlinear least-squares package [38] on a standard desktop environment.

4. Results and discussion

This section is organized into six parts. First, the data reliability was assessed. Second, the experimental gas-phase RTDs were analyzed and compared. Third, the model performance was evaluated across packings and trickling liquid velocities. Fourth, the effects of packing material and liquid velocity on gas-phase dispersion were discussed using Peclet trends. Fifth, the hybrid section-based model and its zone-resolved retention are discussed. Sixth, the limitations and operational considerations are presented.

4.1. Data reliability

4.1.1. Reliability of experimental data

Cross-correlation analysis of the voltage measurements in each set of triplicates yielded high Pearson correlation coefficients ranging from 0.99 to 1.00 (Table S1). These results confirm the dependability of the method and consistency of the measurements over time. Each pulse injection was conducted 30 s after the initiation of the sensor data recording to allow sufficient time to position the syringe in the injection port. The 30 s prior to the injection were excluded from data analysis. Additionally, the measurements of the initial and peak voltages exhibited standard deviations of less than 1 s for all the packing materials tested under all operational conditions. This consistency across triplicates demonstrates the reproducibility of our experimental procedure. Furthermore, the high cross-correlation and low standard deviation of the voltage readings suggest that the selected triplicates reliably represent the data trends observed under the tested conditions. Subsequently, the raw signals were smoothed, and $E(t)$ was computed. Four smoothers were evaluated (Savitzky–Golay, LOWESS, moving average, and a 9th-order polynomial). LOWESS and the 9th-order polynomial performed best; across all packings and TLVs, their fits were nearly identical. To ensure consistency with prior work under similar conditions [18], the 9th-order polynomial was chosen and fitted to 2400 points at $\Delta t = 0.05$ s, achieving $R^2 > 0.99$ for each triplicate (see Table S2 for a comparison of the models). Thus, the voltage readings obtained from the regression model were transformed into concentration values using an R_0 value of 18 kΩ determined based on the calibration curve provided by the manufacturer. All experiments were conducted on the same day using a shared calibration curve, assuming negligible sensor drift throughout the day. Consequently, calibration uncertainty was not considered in the model parameters (e.g., t_m and Pe), and the derived parameters reflected the fixed calibration applied during the data acquisition. This simplification was justified by the implementation of daily pre-calibration and consistent environmental control.

4.1.2. Internal validation and uncertainty quantification

An internal validation analysis was conducted to measure the stability of the hydrodynamic parameters derived from the model calibration and to evaluate the statistical dependability of the fitted descriptors. Residual-based nonparametric bootstrap resampling, as outlined in Section 3.6, was used for each packing material, TLV condition, and model structure. A total of $B = 200$ bootstrap replicates were generated for each case, producing empirical distributions for the mean residence time (t_m), Peclet number (Pe), bed residence time (t_{PBR}), and boundary contributions (t_{B1}, t_{B2}). A summary of the coverage results is presented in Table 1. In all materials and models, the bootstrap 95% confidence intervals (CI_{95}) were relatively narrow compared to their nominal parameter values, with typical widths ranging from ±0.05–0.12 s for t_m and ±0.05–0.6 for Pe. This indicates that the fitted parameters were minimally influenced by experimental variability and the sensitivity of nonlinear regression. The hybrid model consistently showed the smallest CI_{95}, suggesting improved parameter identifiability owing to its explicit representation of boundary and bed contributions. To assess the calibration quality of the asymptotic confidence intervals, empirical coverage values were calculated by comparing the bootstrap distributions with the nominal 95% intervals derived from the covariance matrix of the nonlinear regression. The mean coverage values were close to the nominal target of 0.95 for all packings and parameters, typically ranging from 0.958 to 0.975 for t_m and Pe, and from 0.97 to 1.00 for t_{B1}, t_{B2}, and t_{PBR}. These findings confirm that the asymptotic uncertainty estimates are well-calibrated and that the three models provide statistically consistent parameter estimates. Overall, the bootstrap analysis confirmed that the fitted hydrodynamic parameters were statistically robust and that the models offered well-identified descriptors of gas phase transport under all operating conditions.

Table 1
Mean empirical coverage of nominal 95% asymptotic confidence intervals for the three models across all packings and TLV conditions.

Model	Parameter	CI_{95} Width	Coverage
AD_{cc}+CSTR	t_m	±0.08–0.12 s	0.960
	Pe	±0.30–0.60	0.965
	t_{PBR}	±0.8–1.7 s	0.971
	t_{B1}, t_{B2}	±0.8–1.4 s	0.978
AD_{cc}+PFR	t_m	±0.05–0.10 s	0.964
	Pe	±0.05–0.20	0.972
	t_{PBR}	±0.05–0.10 s	0.978
	t_{B1}, t_{B2}	±0.4–0.8 s	0.985
Hybrid	t_m	±0.05–0.08 s	0.968
	Pe	±0.05–0.15	0.975
	t_{PBR}	±0.05–0.08 s	0.982
	t_{B1}, t_{B2}	±0.3–0.6 s	0.990

4.2. Experimental RTD analysis

The gas residence times across different materials (PUF, spheres, and wood bark) were evaluated under TLV values of 0, 2, 5, and 10 $\text{m}\,\text{h}^{-1}$, denoted as TLV0, TLV1, TLV2, and TLV3, respectively. This is summarized in Table 2 and shown in Fig. 2. When PUF was used as the packing material, the t_m at TLV = $0\,\text{m}\,\text{h}^{-1}$ was 49.77 s, which decreased to 46.39 s at TLV3, representing a 6.8% reduction. The deviation from uniform flow conditions was quantified by the σ_θ^2 value, which ranged from 0.121 at TLV0 to 0.085 at TLV3, indicating improved flow uniformity with increasing TLV. In addition, the rise time (t_{rise}), defined as the time when the sensor first registers a measurement, increased from 21.95 to 25.28 s at TLV2 but decreased at higher values of TLV. The peak time (t_{peak}), which marks the end of the rising phase where the maximum response value is reached, and the end time (t_{end}), which represents the final measurement at the end of the decay phase, consistently decreased as the liquid velocity increased. This suggests an accelerated tracer breakthrough and enhanced dispersion at higher liquid velocities. These observations demonstrate a clear correlation between the liquid velocity and the rate at which the tracer traverses the system. In contrast, the behavior of the spheres exhibited a nonlinear trend in t_m, which increased from 40.77 s at TLV0 to a maximum of 46.61 s at TLV2, before decreasing to 41.38 s at TLV3. This behavior indicates changes in the flow regime due to deviations from the theoretical mean residence time, suggesting a transition between the channeling and dead zones. The increase in TLV reduced the normalized variance from 0.144 to 0.095, suggesting an enhanced flow uniformity. The rise and peak times exhibited a pattern similar to t_m, reaching a maximum at TLV2, whereas the end time decreased from 88.05 to 77.35 s. This phenomenon revealed the sensitivity of the spheres to intermediate TLVs, which is presumably attributable to alterations in the wetting characteristics induced by the modified liquid flow patterns at high velocities, which subsequently influenced gas channeling within the packing. In contrast, wood bark had the shortest t_m among the three packing materials tested, starting at 44.66 s at TLV0 and reducing to 36.97 s at TLV3, a 17.2% decrease in comparison. The normalized variance remained high, ranging from 0.196 to 0 .187, suggesting poor flow uniformity, which may lead to reduced contaminant removal efficiency owing to inadequate residence time distribution and uneven gas–liquid contact. The rise and peak times decreased steadily with increasing TLV, whereas the end time decreased from 103.73 to 84.90 s. This behavior suggests rapid tracer dispersion through the irregular structure of the wood bark, but with considerable flow non-uniformity caused by its heterogeneous packing. Upon examining the normalized variance of the RTD across all materials, the PUF exhibited the most uniform behavior, with $\sigma_\theta^2 = 0.121$ at TLV0 and decreasing to 0.085 at TLV3. Conversely, the Tri-Pack spheres displayed broader RTD curves, with σ_θ^2 ranging from 0.144 to 0.095. Wood bark demonstrated the lowest uniformity, maintaining a high σ_θ^2 value across all TLVs. These differences can be attributed to the structural and hydrodynamic characteristics of the material. The heterogeneous structure of wood bark, along with its water retention capability (40%–60%) [27], likely contributed to the formation of tortuous pathways for gas flow, as the adsorbed water reduces the internal flow path within the wood bark. In contrast, the PUF and Tri-Pack spheres exhibited different behaviors. Despite their similar porosities, the spheres channeled the gas significantly faster than the PUF at TLV3.

Table 2
Experimental results for different materials obtained by triplicates.

Material	TLV [m h^{-1}]	t_m [s]	σ_θ^2 [–]	t_{rise} [s]	t_{peak} [s]	t_{end} [s]
PUF	0	49.77 ± 0.66	0.121 ± 0.006	21.95 ± 0.20	38.28 ± 0.88	101.98 ± 2.62
	2	49.20 ± 0.59	0.087 ± 0.001	25.03 ± 0.10	36.17 ± 1.64	91.35 ± 1.53
	5	47.98 ± 0.79	0.076 ± 0.002	25.28 ± 0.23	38.33 ± 2.87	85.62 ± 0.93
	10	46.39 ± 0.02	0.085 ± 0.001	23.23 ± 0.15	35.62 ± 0.30	85.47 ± 0.36
Tri-Packs spheres	0	40.77 ± 0.44	0.144 ± 0.001	14.28 ± 0.13	29.17 ± 0.40	86.87 ± 0.93
	2	44.51 ± 0.91	0.095 ± 0.005	18.12 ± 1.63	36.62 ± 1.89	81.72 ± 1.46
	5	46.61 ± 0.42	0.101 ± 0.001	18.62 ± 0.40	38.87 ± 0.50	88.05 ± 1.18
	10	41.38 ± 0.53	0.095 ± 0.001	17.80 ± 0.33	34.23 ± 0.46	77.35 ± 0.43
Wood bark	0	44.66 ± 0.09	0.196 ± 0.009	11.77 ± 0.38	30.83 ± 0.83	103.73 ± 1.98
	2	42.81 ± 0.15	0.163 ± 0.003	12.92 ± 0.29	32.13 ± 1.53	92.80 ± 0.63
	5	40.47 ± 0.45	0.165 ± 0.007	12.33 ± 0.35	29.48 ± 0.86	88.32 ± 1.21
	10	36.97 ± 0.64	0.187 ± 0.001	10.02 ± 0.21	24.83 ± 1.14	84.90 ± 1.63

Table 3
Model comparison parameters for polyurethane foam packing. The best R^2 (max) and AIC/BIC (min) values for each TLV are bolded. Deltas are computed within each TLV block as $\Delta\text{AIC} = \text{AIC}_i - \min(\text{AIC})$, $\Delta\text{BIC} = \text{BIC}_i - \min(\text{BIC})$, and $\Delta R^2 = \max(R^2) - R_i^2$. Parameter estimates are reported as "value ± SE", where SE denotes the standard error obtained from the asymptotic covariance matrix of the nonlinear least-squares fit; SEs for t_m are computed by propagating this covariance via the delta method.

TLV [m h^{-1}]	Model	Pe	t_m [s]	t_{B1} [s]	t_{B2} [s]	t_{PBR} [s]	R^2	AIC	BIC	ΔAIC	ΔBIC	ΔR^2
0	AD$_{cc}$+CSTR	22.12 ± 2.14	50.62 ± 1.14	16.53 ± 0.77	10.08 ± 0.81	24.01 ± 0.21	0.96	−30830.88	−30807.74	2053.90	2053.91	0.02
	AD$_{cc}$+PFR	4.37 ± 1.48	53.33 ± 1.66	9.14 ± 1.29	3.36 ± 1.04	40.83 ± 0.17	0.97	−31480.83	−31457.70	1403.95	1403.95	0.01
	Hybrid	11.14 ± 1.09	52.49 ± 1.48	15.71 ± 0.74	15.70 ± 1.27	21.08 ± 0.19	**0.98**	**−32884.78**	**−32861.65**	0.00	0.00	0.00
2	AD$_{cc}$+CSTR	19.49 ± 1.73	50.03 ± 0.74	13.78 ± 0.68	3.36 ± 0.24	32.89 ± 0.17	0.96	−30026.95	−30003.82	1538.10	1538.10	0.02
	AD$_{cc}$+PFR	6.73 ± 0.63	51.36 ± 3.76	8.14 ± 0.47	5.25 ± 0.37	37.97 ± 0.19	0.97	−30641.67	−30618.54	923.38	923.38	0.01
	Hybrid	18.07 ± 1.65	51.88 ± 1.21	13.65 ± 0.68	13.65 ± 0.98	24.65 ± 0.12	**0.98**	**−31565.05**	**−31541.92**	0.00	0.00	0.00
5	AD$_{cc}$+CSTR	18.46 ± 2.77	48.44 ± 1.02	10.00 ± 0.93	3.36 ± 0.39	35.08 ± 0.16	0.97	−29961.55	−29938.42	824.56	824.56	0.01
	AD$_{cc}$+PFR	9.10 ± 5.32	49.64 ± 4.88	5.51 ± 0.37	5.98 ± 3.44	38.15 ± 0.21	0.97	−30371.95	−30348.81	414.16	414.17	0.01
	Hybrid	21.94 ± 3.43	50.73 ± 1.94	12.77 ± 1.21	12.80 ± 1.51	25.18 ± 0.12	**0.98**	**−30786.11**	**−30762.98**	0.00	0.00	0.00
10	AD$_{cc}$+CSTR	15.89 ± 1.73	46.92 ± 0.76	10.41 ± 0.68	3.36 ± 0.29	33.15 ± 0.16	0.97	−30159.85	−30136.72	854.11	854.10	0.01
	AD$_{cc}$+PFR	9.10 ± 3.30	48.04 ± 1.55	5.70 ± 1.08	3.55 ± 1.09	38.75 ± 0.20	0.97	−30549.19	−30526.06	464.77	464.76	0.01
	Hybrid	20.08 ± 2.27	49.13 ± 1.42	12.99 ± 0.86	12.99 ± 1.13	23.17 ± 0.11	**0.98**	**−31013.96**	**−30990.82**	0.00	0.00	0.00

This disparity was primarily attributed to the small pore size of the PUF, which allowed the formation of water patches inside the porous bed, and the low gas velocity was insufficient to disrupt the surface tension effect [39]. PUF, which are characterized by low permeability, lead to a significant pressure drop that hinders liquid passage through the medium. Water retention within the PUF generated a considerable opposing force that could not be overcome by the available gas velocity. Consequently, the gas cannot effectively displace the trapped liquid, leading to obstructed or significantly reduced gas flow. This behavior suggests that in practical applications, the deformation or compression of the PUF is governed less by pressure-induced stresses and more by the dominance of the immobile liquid phase, which alters the internal flow dynamics of the porous matrix [40].

4.3. Models performance

The model performance was assessed across three packings and four trickling liquid velocities (TLV0–TLV3) using R^2, AIC, and BIC (Tables 3–5) and is illustrated in Fig. 3. For the polyurethane foam packing (Table 3), the hybrid model was consistently selected as the best model for all TLVs. This outcome is consistent with the high porosity and large specific surface area of the open–cell foam, where the inlet and outlet redistribution and local recirculation are expected nonidealities that cannot be captured by a single mixed zone. In addition, the time–scale parameters offer a physically interpretable partition of the mean residence time. For all TLVs, the additivity $t_{B1} + t_{PBR} + t_{B2} \approx t_m$ was satisfied, with $t_{B1} \approx t_{B2}$ and t_{PBR} accounting for the central convective–dispersive transport. As TLV increased, $t_{B1} + t_{B2}$ decreased, whereas t_{PBR} slightly increased, suggesting that the liquid velocity reduced the holdup/mixing in the buffer zones more than it altered the packed bed transport. However, at TLV = $10\,\text{m}\,\text{h}^{-1}$, a small reversal in t_{PBR} was observed, which is consistent with diminishing returns at very high trickling rates.

For the spheres (Table 4), the AD$_{cc}$+CSTR model provided the best fit when the liquid phase was present (TLV1–TLV3), whereas the hybrid model was selected for the dry case (TLV0). Thus, even modest trickling liquid velocities simplified the hydrodynamics to an axial dispersion core with a single, dominant mixed region. The fitted time scales again closed the time budget ($t_{B1} + t_{PBR} + t_{B2} \approx t_m$), and for TLV1–TLV3 a near–perfect symmetry $t_{B1} \approx t_{B2}$ was obtained (e.g., $t_{B1} = t_{B2} = 7.74$–8.78 s), while t_{PBR} decreased slightly with increasing TLV, indicating a progressive shift towards plug–flow behavior under liquid recirculation. This trend is consistent with reports that modest liquid velocities improve wetting and mitigate channeling in packed beds and biofilters, thereby shifting the gas RTD towards plug flow [21].

For wood bark packing (Table 5), the selected model varied with TLV: the hybrid model was favored for TLV0, TLV2, and TLV3, whereas AD$_{cc}$+CSTR was preferred for TLV1. The need for two mixed zones in three of the four cases indicates persistent nonidealities, likely related to the irregular geometry and heterogeneous wettability of the wood bark, which were only partially mitigated by the liquid recirculation. The fitted time scales again partitioned the mean residence time, with $t_{B1} \approx t_{B2}$ across all hybrid–selected cases and a clear decrease in $t_{B1} + t_{B2}$ as the TLV increased, indicating reduced buffer zone holdup with higher TLVs, whereas t_{PBR} remained comparatively smaller than in the synthetic packings, consistent with stronger overall dispersion in the wood bed.

Across all materials and TLVs, the model employing PFR behavior for the buffer zones (i.e., AD$_{cc}$+PFR) systematically yielded inferior fits (higher AIC/BIC and/or lower R^2). Therefore, the vessel regions immediately below and above the packed bed cannot be assumed to behave as ideal plug-flow segments. This outcome is consistent with the expected hydrodynamics when the gas inlet is placed on the side of the reactor, where recirculation and mixing in the disengagement space are promoted [18].

Table 4
Model comparison parameters for spheres packing. The best R^2 (max) and AIC/BIC (min) values per TLV are bolded. Deltas are computed within each TLV block as $\Delta\text{AIC} = \text{AIC}_i - \min(\text{AIC})$, $\Delta\text{BIC} = \text{BIC}_i - \min(\text{BIC})$, and $\Delta R^2 = \max(R^2) - R_i^2$. Parameter estimates are reported as "value ± SE", where SE denotes the standard error obtained from the asymptotic covariance matrix of the nonlinear least-squares fit; SEs for t_m are computed by propagating this covariance via the delta method.

TLV [m h^{-1}]	Model	Pe	t_m [s]	t_{B1} [s]	t_{B2} [s]	t_{PBR} [s]	R^2	AIC	BIC	ΔAIC	ΔBIC	ΔR^2
0	AD_{cc}+CSTR	20.01 ± 0.84	42.31 ± 0.49	15.44 ± 0.35	10.08 ± 0.33	16.79 ± 0.07	0.98	−32393.93	−32370.80	642.16	642.16	0.01
	AD_{cc}+PFR	4.37 ± 0.53	43.65 ± 0.51	5.51 ± 0.34	3.36 ± 0.35	34.78 ± 0.13	0.98	−31539.94	−31516.81	1496.15	1496.15	0.01
	Hybrid	8.23 ± 0.36	43.34 ± 0.58	14.27 ± 0.32	14.10 ± 0.48	14.97 ± 0.06	**0.99**	**−33036.09**	**−33012.96**	0.00	0.00	0.00
2	AD_{cc}+CSTR	11.47 ± 0.90	45.83 ± 0.76	7.74 ± 0.46	7.74 ± 0.35	30.36 ± 0.5	**0.98**	**−31936.43**	**−31913.30**	0.00	0.00	0.00
	AD_{cc}+PFR	7.92 ± 2.06	47.47 ± 1.07	5.51 ± 0.74	3.36 ± 0.75	38.60 ± 0.20	0.97	−30435.51	−30412.38	1500.92	1500.92	0.01
	Hybrid	15.01 ± 2.31	48.78 ± 2.54	15.58 ± 1.76	20.42 ± 1.81	15.80 ± 0.27	0.95	−29501.86	−29478.73	2434.57	2434.57	0.03
5	AD_{cc}+CSTR	11.47 ± 0.51	47.72 ± 0.56	8.78 ± 0.26	8.78 ± 0.23	30.16 ± 0.43	**0.98**	**−32366.87**	**−32343.74**	0.00	0.00	0.00
	AD_{cc}+PFR	6.73 ± 2.47	50.05 ± 1.54	5.72 ± 1.08	3.47 ± 1.05	40.86 ± 0.19	0.97	−31090.23	−31067.10	1276.64	1276.64	0.01
	Hybrid	14.13 ± 0.43	50.61 ± 0.48	14.87 ± 0.24	14.81 ± 0.27	20.93 ± 0.31	0.96	−30305.70	−30282.56	2061.17	2061.18	0.02
10	AD_{cc}+CSTR	13.84 ± 4.23	42.08 ± 2.39	7.97 ± 1.60	7.97 ± 1.77	26.15 ± 0.14	**0.98**	**−31716.97**	**−31693.84**	0.00	0.00	0.00
	AD_{cc}+PFR	7.92 ± 1.39	43.42 ± 0.73	5.51 ± 0.50	3.36 ± 0.51	34.55 ± 0.16	0.98	−30980.24	−30957.11	736.73	736.73	0.00
	Hybrid	15.02 ± 3.30	44.39 ± 2.64	12.48 ± 1.64	12.54 ± 2.06	19.37 ± 0.24	0.97	−30350.66	−30327.53	1366.31	1366.31	0.01

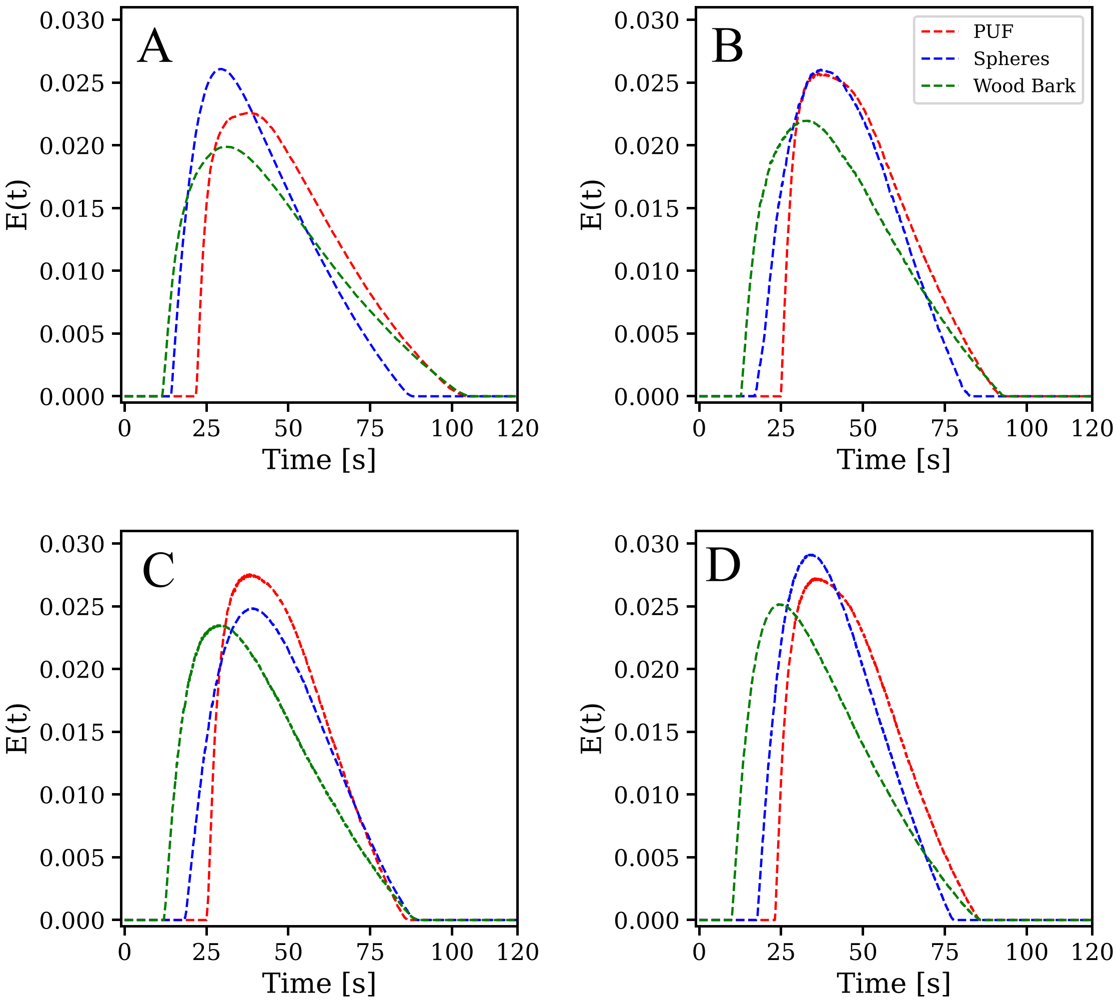

Fig. 2. Experimental gas-phase RTD for the selected packing at four trickling liquid velocities (TLV): (A) 0, (B) 2, (C) 5, and (D) 10 m h^{-1}.

All three models demonstrated high R^2 values against the experimental RTD, accurately capturing both the peak time and height with minimal residuals. A limitation arises from the sensor's lower detection threshold (~500 ppmv), which truncates the late-time tail. In such instances, the fitted model can be employed to extrapolate the unobserved tail mass [18]. To bound the truncation bias, a model-based tail was appended beyond the acquisition window by extending the fitted hybrid response to $10\,t_m$ and integrating the remainder. In a representative case (PUF–TLV0, Hybrid), the appended tail contributed 1.25% of RTD mass and increased t_m from 52.49 to 53.57 s (Δ = 2.06%). The fitted parameters and model selection (ΔAIC/ΔBIC/ΔR^2) were unaffected, as the tail was used solely for moment correction. However, by improving the sensitivity of the sensor and obtaining the tail of the experimental RTD curve, the three models will not be able to represent the stagnation within the trickle bed because they do not consider this phenomenon. In this case, a model that considers dynamic

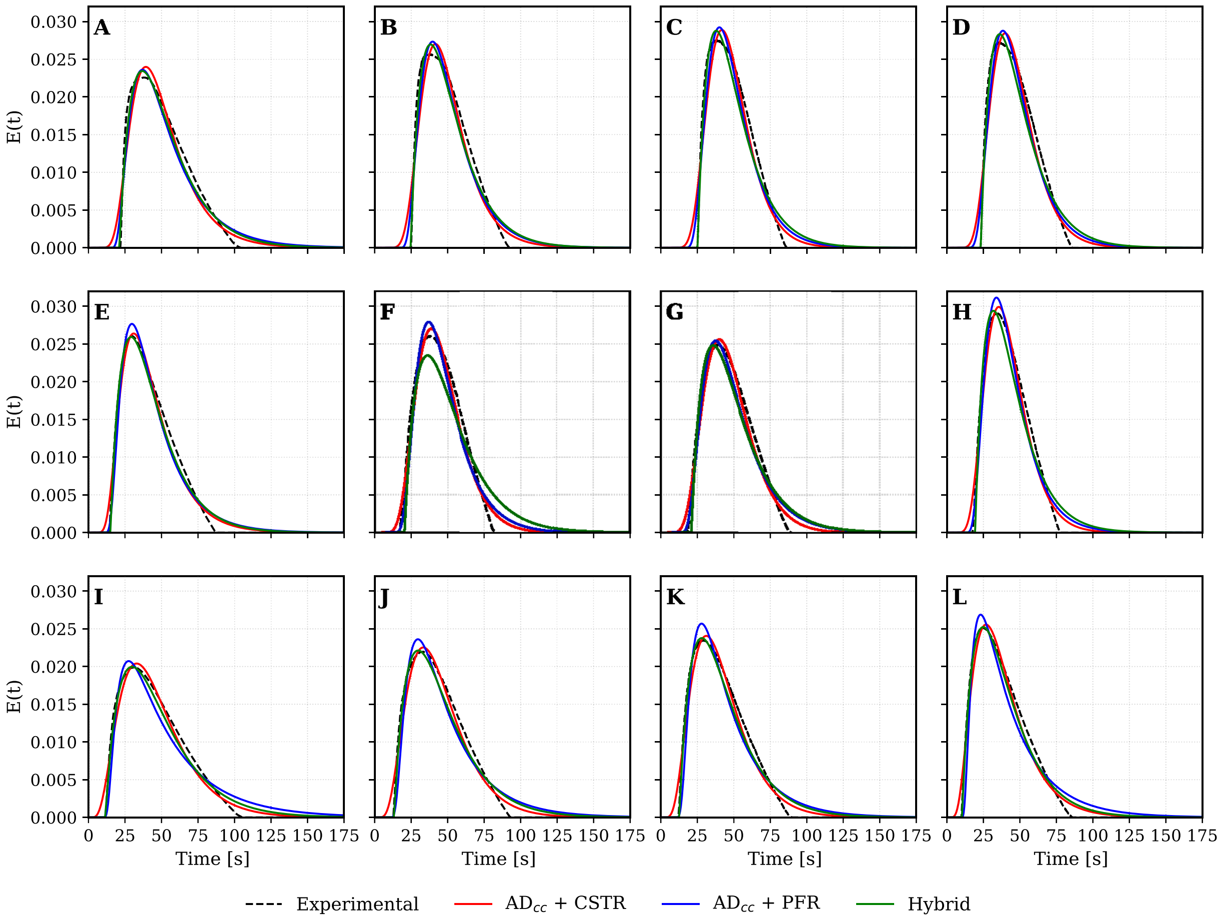

Fig. 3. Experimental RTD data (black dashed) compared with three models: AD$_{cc}$+CSTR (red), AD$_{cc}$+PFR (blue), and Hybrid (green). Panels A–D: Polyurethane Foam at TLV = 0, 2, 5, and 10 m h^{-1} E–H: Tri-Packs spheres at TLV = 0, 2, 5, and 10 m h^{-1}. I–L: Wood bark at TLV = 0, 2, 5, and 10 m h^{-1}.

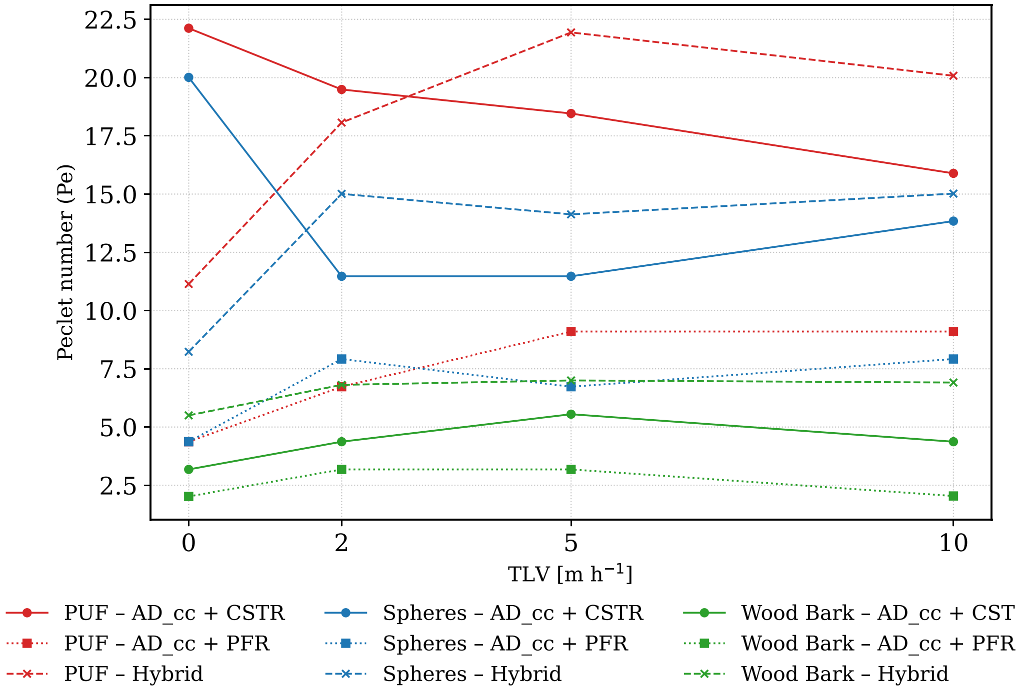

Fig. 4. Best–fit Peclet number versus trickling liquid velocity (TLV) at constant gas flow (8 L min^{-1}) for three packing materials: polyurethane foam (PUF), Tri–Packs spheres, and wood bark. Curves correspond to the three RTD models shown in the legend—Model A (AD$_{cc}$+CSTR), Model B (AD$_{cc}$+PFR), and the Hybrid model.

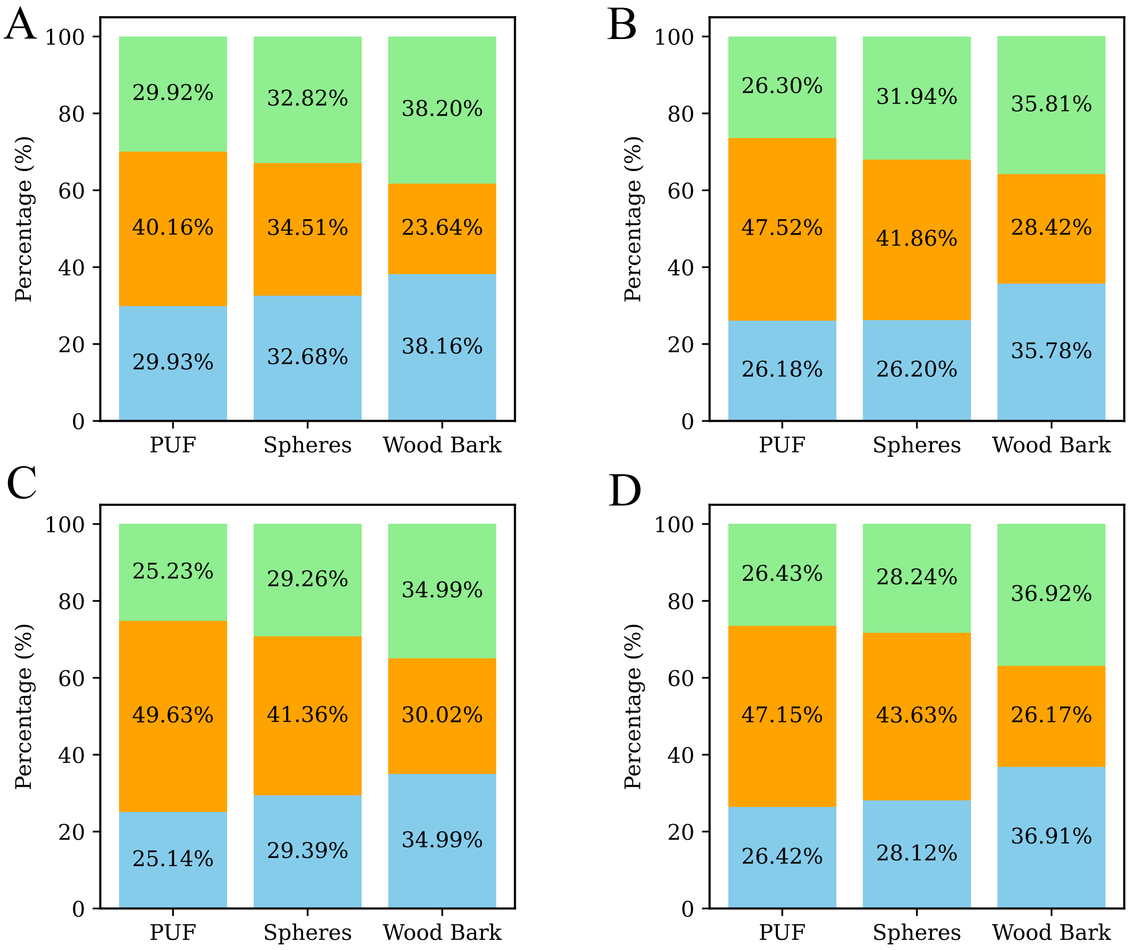

Fig. 5. Distribution of the global mean residence time of gas in different reactor zones. The blue, orange, and green segments represent the empty volume below the packed bed zone, the packed bed zone, and the empty volume above the packing zone, respectively. The subfigures illustrate the results for the varying TLVs. (A) TLV = 0 m h^{-1}, (B) TLV = 2 m h^{-1}, (C) TLV = 5 m h^{-1}, and (D) TLV = 10 m h^{-1}.

Table 5
Model comparison parameters for wood bark packing. The best R^2 (max) and AIC/BIC (min) per TLV are bolded. Deltas are computed within each TLV block as $\Delta\mathrm{AIC} = \mathrm{AIC}_i - \min(\mathrm{AIC})$, $\Delta\mathrm{BIC} = \mathrm{BIC}_i - \min(\mathrm{BIC})$, and $\Delta R^2 = \max(R^2) - R_i^2$. Parameter estimates are reported as “value ± SE”, where SE denotes the standard error obtained from the asymptotic covariance matrix of the nonlinear least-squares fit; SEs for t_m are computed by propagating this covariance via the delta method.

TLV [m h^{-1}]	Model	Pe	t_m [s]	t_{B1} [s]	t_{B2} [s]	t_{PBR} [s]	R^2	AIC	BIC	ΔAIC	ΔBIC	ΔR^2
0	AD$_{cc}$+CSTR	3.18 ± 0.32	45.99 ± 1.17	16.53 ± 0.53	10.08 ± 0.89	19.38 ± 0.54	0.98	−32611.29	−32588.15	1117.51	1117.52	0.00
	AD$_{cc}$+PFR	2.02 ± 0.27	52.94 ± 0.59	5.51 ± 0.38	3.36 ± 0.38	44.07 ± 0.23	0.95	−30707.74	−30684.61	3021.06	3021.06	0.03
	Hybrid	5.50 ± 1.89	48.29 ± 5.77	18.43 ± 1.71	18.47 ± 5.41	11.41 ± 1.01	**0.98**	**−33728.80**	**−33705.67**	0.00	0.00	0.00
2	AD$_{cc}$+CSTR	4.37 ± 0.97	44.13 ± 2.37	12.04 ± 1.45	10.08 ± 1.81	22.01 ± 0.51	**0.98**	**−32285.23**	**−32262.10**	0.00	0.00	0.00
	AD$_{cc}$+PFR	3.18 ± 0.55	48.29 ± 0.73	5.51 ± 0.49	3.36 ± 0.50	39.42 ± 0.21	0.95	−30200.48	−30177.35	2084.75	2084.75	0.03
	Hybrid	6.81 ± 1.46	46.46 ± 3.36	16.64 ± 1.76	16.63 ± 2.81	13.20 ± 0.33	0.98	−32081.56	−32058.43	203.67	203.67	0.00
5	AD$_{cc}$+CSTR	5.55 ± 0.86	41.57 ± 1.67	13.25 ± 1.04	10.08 ± 1.26	18.24 ± 0.34	0.98	−32103.48	−32080.35	342.04	342.04	0.00
	AD$_{cc}$+PFR	3.18 ± 0.45	45.07 ± 0.60	5.51 ± 0.41	3.36 ± 0.40	36.20 ± 0.18	0.96	−30198.18	−30175.05	2247.34	2247.34	0.02
	Hybrid	7.00 ± 0.78	43.57 ± 1.63	15.48 ± 0.80	15.48 ± 1.40	12.61 ± 0.19	**0.98**	**−32445.52**	**−32422.39**	0.00	0.00	0.00
10	AD$_{cc}$+CSTR	4.37 ± 0.98	38.34 ± 1.44	14.91 ± 0.47	3.36 ± 0.71	20.07 ± 1.17	0.98	−32279.98	−32256.84	954.95	954.96	0.01
	AD$_{cc}$+PFR	2.04 ± 0.18	42.61 ± 0.37	5.51 ± 0.23	3.36 ± 0.23	33.74 ± 0.18	0.95	−29942.51	−29919.38	3292.42	3292.42	0.04
	Hybrid	6.91 ± 0.99	39.46 ± 1.90	14.58 ± 0.85	14.58 ± 1.63	10.33 ± 0.48	**0.99**	**−33234.93**	**−33211.80**	0.00	0.00	0.00

and stagnant zones and mass exchange between them will be required, such as the plug dispersion exchange (PDE) model [41,42], which will be the topic of future studies.

4.4. Effect of packing material and liquid velocity on gas-phase dispersion

To quantify the impact of the TLV on gas-phase mixing, the Peclet number from the best model for each condition was evaluated. The results are shown in Fig. 4. For polyurethane foam, Pe increased from ≈ 11.1 at (TLV0) to ≈ 18.1 (TLV1) and ≈ 21.9 (TLV2), followed by a slight decrease to ≈ 20.1 (TLV3). Moderate trickling rates (2–5 m h^{-1}) were found to significantly reduce axial dispersion. However, increasing the rate to 10 m h^{-1}resulted in diminishing or slightly negative effects, suggesting that the distribution of liquid within the packing enhances gas channeling inside the packing [21,39]. For the spheres, an increase from $Pe \approx 8.2 - 13.8$. was observed. In contrast to PUF packing, this suggests that wetting effectively suppresses preferential gas pathways and wall effects in this structured packing, progressively shifting the RTD towards plug flow as the TLV increases. However, the Pe obtained from the PUF was higher than that obtained from the spheres for all conditions. In the case of wood bark, Pe exhibited a non-monotonic pattern: it began at $Pe \approx 5.5$ (TLV0), decreased to approximately 4.4 (TLV1), and subsequently increased to approximately 7.0 (TLV2) and 6.9 (TLV3). This suggests that at higher flow rates, more uniform wetting diminishes uneven wetting, resulting in a higher Pe. Under all conditions, wood bark consistently demonstrated the lowest Pe among the three packings, indicating a stronger dispersion and larger effective mixing volume. This behavior is consistent with previous findings for rough and heterogeneous biofilter media [16]. These trends collectively suggest that TLV affects gas-phase dispersion differently, depending on the type of packing material. PUF and spheres demonstrated notable improvements under conditions of modest to moderate TLVs, whereas wood bark required higher TLVs to counteract its inherent heterogeneity. Importantly, for all three types of packing, an increase in TLV from approximately 5 to 10 $\mathrm{m\,h^{-1}}$ resulted in a negligible change in the Pe number, indicating diminishing returns beyond approximately 5 $\mathrm{m\,h^{-1}}$. These findings underscore the importance of selecting appropriate packing materials and adjusting the TLV to guide the gas RTD towards the desired hydrodynamic regime.

4.5. Hybrid section–based model analysis

In this section, the hybrid model was used to interpret the zone-resolved retention across all packings and TLVs. Fig. 5 shows the fractions of the global mean residence time assigned to the lower buffer (t_{B1}, blue), packed bed (t_{PBR}, orange), and upper buffer (t_{B2}, green) buffers. At TLV0 (panel A), the PUF directed 40.16% of the time to the bed, with the remainder split almost symmetrically between the buffers. Spheres exhibited a more even three–way partition (32.82%–34.51%–32.68%), whereas wood bark showed the smallest contribution to the packed bed (23.64%) and the largest to the buffers (38.2%–38.16%). As the TLV increased (panels B–D), the bed retention time for PUF increased from 40.2% (TLV0) to 49.6% (TLV2), followed by a slight decline at TLV3 (47.1%). The spheres exhibited a consistent increase from 34.5% (TLV0) to 43.6% (TLV3). The wood bark content increased from 23.6% (TLV0) to 30.0% (TLV2) and subsequently decreased to TLV3 (26.2%). In all instances, the buffer contributions remained nearly symmetric ($t_{B1} \approx t_{B2}$), which aligns with the presence of mixed disengagement spaces above and below the bed rather than ideal plug–flow segments, as anticipated for side–entry gas configurations [18]. Compared with Model A (AD$_{cc}$+CSTR), the hybrid model provided more time to the lower and upper buffers (t_{B1} and t_{B2}) and less time to the packed bed (t_{PBR}). This caused the dispersion measured by Pe to be more focused on the beds. The boundary hold-up is denoted by t_{B1} and t_{B2}, leading to a lower and more packed bed-focused Pe. For example, for spheres at TLV0, hybrid Model A estimated $Pe = 8.23$, whereas Model B estimated $Pe = 20.01$. Both models had similar fit quality, but the hybrid model showed that most of the curve broadening was due to boundary mixing and not the bed effect. The trends with TLV support that with moderate TLV, polyurethane foam and spheres have larger bed contributions (higher t_{PBR} fraction) and less buffer hold-up. In contrast, wood bark maintained more buffer contributions and had a smaller t_{PBR}, indicating ongoing nonidealities.

In summary, the results of the hybrid model indicate that the temporal contributions of the buffer and packed-bed zones systematically vary with the packing type and TLV, and these hydrodynamic signatures correspond to the observed performance trade-offs between the materials. At TLV0, the polyurethane foam demonstrated a relatively balanced distribution between the packed bed ($\approx$ 41%) and buffers ($\approx$ 59%), whereas the spheres exhibited a near three-way partition among zones. In contrast, wood bark displayed a predominantly buffer-dominated profile, with only $\approx$ 24% of the residence time allocated to the main bed. As TLV increased, foam and spheres progressively shifted their residence time towards the bed, suggesting enhanced plug-flow characteristics, whereas wood bark maintained a high buffer contribution across all flow rates, indicating persistent maldistribution or dead-zone formation. Consistent with these patterns, the PUF exhibited the highest gas residence times and Pe numbers across all TLVs, indicating plug-flow-like conditions with reduced axial dispersion. Such conditions can enhance gas-biofilm contact for low loads or slowly degrading pollutants; however, they are often accompanied by higher pressure drops in foam-based media [16,39]. Conversely, the spheres presented relatively shorter residence times and smaller Pe values, favoring high-throughput operations in which energy efficiency and hydraulic stability are prioritized. Although wood bark is appealing as a natural medium, it exhibits high variance sensitivity to TLV and a persistently large buffer fraction, reflecting a greater flow variability than other materials. This segmentation also offers a measurable improvement in interpretation compared with ADM-based methods. For example, at TLV0 with spheres, the comparison between the axial dispersion models and the hybrid model shows a reduction of more than 50% in the apparent axial dispersion when buffers are not included in the core flow area. This discrepancy has direct design implications: sizing a reactor based on the ADM-derived Pe would assume significantly lower mixing and could overestimate the conversion efficiency or under-design the bed length. By attributing much of the RTD broadening to stagnant boundary zones, the hybrid model offers a more accurate basis for predicting plug-flow behavior. Overall, these distinctions underscore the design trade-offs between contact time, flow uniformity, and operational demands that must be considered when selecting the packing materials for gas-phase biofiltration.

Although the hybrid model generally provided the best overall description of the RTD data, there were specific operating conditions in which it did not outperform the AD$_{cc}$+CSTR formulation. This behavior was predominantly observed for spherical packing at intermediate TLVs, where the RTD profiles exhibited sharp peaks and limited evidence of zone-dependent dispersion. Under these conditions, gas-phase transport is expected to be dominated by near-plug-flow motion through uniform interstitial voids, with only a minor contribution from localized mixing regions. Because the hybrid model explicitly separates the bed and boundary subdomains, its advantage diminishes when the characteristic mixing intensity in the boundary region becomes negligible or indistinguishable from that of the bulk region. In contrast, the AD$_{cc}$+CSTR model can reproduce these narrow RTDs using a single effective mixing parameter, without incurring additional structural complexities. This observation suggests a practical guideline for model selection: when the measured RTD exhibits a pronounced peak with $Pe \gtrsim 10$ and a normalized variance indicative of near-plug-flow behavior ($\sigma^2/t_m^2 < 0.05$), a single-zone model such as AD$_{cc}$+PFR or AD$_{cc}$+CSTR is adequate for estimating the parameters. Conversely, when it is necessary to account for spatially heterogeneous mixing, whether due to a lower Pe, the presence of regions with distinct local dispersion, or the existence of multiple characteristic transport times, the hybrid model is the more suitable option. This guideline illustrates the hydrodynamic behavior of different types of packing; spherical media tend to create relatively consistent flow channels with minimal spatial variation in the mixing. In contrast, other packings, such as PUF or wood-based structures, have distinctly unique void architectures that form localized areas with varying dispersion characteristics, thus benefiting from multizone representation.

The hydrodynamic trends identified in this study, particularly the axial dispersion variation and buffer contributions quantified by the hybrid model, qualitatively align with those of recent studies utilizing CFD. Particle-resolved CFD simulations have demonstrated that packed beds inherently develop preferential gas pathways and recirculating eddies, particularly near the walls or when the bed-to-particle diameter ratio is low, leading to maldistribution and underutilized zones [43]. These characteristics correspond to the increased buffer fractions and reduced effective Peclet numbers observed in the wood-bark system. Furthermore, Lovreglio et al. [44] showed that even at high flow rates, stagnant hold-up zones persist and contribute to RTD tailing, corroborating the long residence time behavior captured by the sensor-derived RTD curve. These effects were evident in our results, as consistently large buffer times were observed in the wood-packed column for all the TLVs. In practice, the hybrid model illustrated in Fig. 5 can be used to identify buffer zones under real operating conditions. Because the Pe number and buffer residence time contributions respond to hardware changes, they can be used to minimize buffer volumes at the pilot scale by iterating header baffles and distributor layouts until Pe and t_m stabilize. This methodology aligns with standard practice, as calibration conducted on the day of use under stable ambient conditions minimizes drift. Moreover, the sensing component was engineered to be easily replaceable on the Arduino platform, with each unit costing less than $20. This design supports economical, real-time hydrodynamic monitoring and allows for quick maintenance during the scaling-up phase.

4.6. Limitations and operational considerations

This study presents a hydrodynamic analysis based on residence time distribution utilizing a metal oxide (MOx) gas sensor in packed beds under gas phase operation. Although the proposed methodology is informative and adaptable, it is subject to several assumptions and limitations that should be considered.

- **MOx sensor response and calibration:** The MOx sensor demonstrates a non-instantaneous response and limited linearity. Despite the application of lag compensation and baseline correction, its sensitivity to ambient humidity, temperature drift, and extended tracer pulses may introduce potential bias in the estimation of early arrival times or RTD tails. In addition, the presence of water may affect the sensitivity of the sensor, making it unreliable in describing the gas phase flow pattern.
- **Tracer injection reproducibility:** The pulse injection protocol was manually executed, potentially introducing minor variations in duration and volume. This can affect the sharpness of the response curve, particularly at low velocities and under high-dispersion conditions.
- **Simplifying assumptions in modeling:** The hybrid model represents the reactor as a combination of idealized continuous stirred-tank reactor (CSTR) and axial dispersion zones, which facilitates interpretability but does not fully capture three-dimensional flow phenomena or localized effects such as bypass jets or dead zones.
- **No spatial resolution of internal flow fields:** The methodology provides a temporal signal at the outlet but does not capture local voidage, internal velocities, or cross-sectional dispersion. Consequently, detailed hydrodynamic features, such as radial gradients or wall effects, were not resolved.
- **Tail truncation under prospective biofilm growth:** The current dataset was obtained without biofilm. In future scenarios where packings are covered with biofilms, increased tortuosity and localized stagnation are expected to prolong tracer residence times and emphasize far tails in RTD. To address this situation, the methodology should be adjusted to prevent apparent baseline truncation, such as by increasing the tracer dose, extending the acquisition window, and/or expanding the detector dynamic range. Integrating MOx sensing with a secondary method (e.g., gas chromatography) is anticipated to recover late-stage signals from slow-exchanging zones, thereby extending the measurable tail when biofilms are present.

Given these limitations, the selection of alternative diagnostics depends on the complexity of the system and the information requirements.

- **Computational Fluid Dynamics (CFD)** is recommended for investigating small-scale flow heterogeneity, packing-induced channeling, or distributor effects. It is particularly suited for scale-up studies and the structural optimization of complex geometries.
- **Electrical Resistance Tomography (ERT)** is appropriate for resolving gas-liquid distribution, phase holdup, and flow regime shifts in multiphase or non-transparent reactors. It can also assist in detecting regions with prolonged stagnation periods.
- **Particle Image Velocimetry (PIV)** provides high-resolution velocity field data and is ideal for validating flow regimes and quantifying wake structures. However, its application is constrained by the need for transparent reactor walls, ambient conditions, and expensive, high-speed optical equipment, rendering it impractical for opaque or industrial-scale systems.

5. Conclusions

This study demonstrated the key role of packing material and gas-liquid flow conditions in the hydraulic behavior of packed bed reactors. The PUF exhibited superior hydraulic performance, characterized by reduced axial dispersion and predictable flow patterns, making it particularly suitable for applications that require a uniform gas residence time. In contrast, wood bark exhibited the most pronounced deviations from plug flow, driven by its irregular structure and poor ability to sustain uniform flow dynamics. The spheres exhibited intermediate behavior, balancing the flow uniformity and retention. At the level of model discrimination, the hybrid formulation minimized the information criteria for PUF at all liquid velocities and for wood bark at low velocities, whereas the AD_{cc}+CSTR variant matched or outperformed the hybrid model for spheres at intermediate and high velocities. In addition, the buffer zone residence times recovered by the hybrid model were generally of similar magnitude, supporting a near-symmetrical mixing contribution from the entry and exit regions of the buffer zone. On a practical level, this systematic RTD modeling effectively characterizes gas-phase hydrodynamics; however, it is inadequate for addressing localized structures, such as eddies, channeling, and microscale turbulence. Although CFD can capture these details [39], its computational requirements limit its application in routine analysis. Techniques such as ERT and PIV, despite offering spatial resolution, encounter cost and operational challenges. In this context, the MOx-sensor-based RTD methodology, when integrated with different candidate models, presents a scalable and cost-effective alternative for analyzing gas-phase dispersion in this type of reactor system. It effectively identifies deviations from the optimal flow, addresses packing-specific effects on gas transport, and offers actionable diagnostics for the evaluation of the reactor. Future research should aim to validate these trends on a pilot scale and under conditions that support sustained biofilm growth. When necessary, section-based modeling should be integrated with spatial diagnostics or CFD to accurately identify channeling, dead zones, and boundary recirculation while balancing experimental and computational costs. This integration enhances the reproducibility of simulation-based approaches and broadens the applicability of the findings to various reactor configurations.

CRediT authorship contribution statement

Felipe A. Carreño-López: Writing – review & editing, Writing – original draft, Visualization, Validation, Software, Methodology, Investigation, Formal analysis, Data curation, Conceptualization. **Patricio A. Moreno-Casas:** Writing – review & editing, Visualization, Supervision, Resources, Project administration, Funding acquisition, Formal analysis. **Felipe Scott:** Writing – review & editing, Validation, Methodology, Funding acquisition, Formal analysis, Conceptualization. **Alberto Vergara-Fernández:** Writing – review & editing, Supervision, Resources, Funding acquisition, Formal analysis. **José Sierra-Pallares:** Writing – review & editing, Validation, Methodology, Investigation, Formal analysis. **Raúl Muñoz:** Writing – review & editing, Supervision, Resources, Project administration, Funding acquisition, Formal analysis, Conceptualization.

Declaration of competing interest

All authors declare that no conflict of interest exists.

Acknowledgments

The authors gratefully acknowledge the financial support provided by the Spanish Research Agency through Project PLEC2022-009349. This research was also funded by the Agencia Nacional de Investigación *y* Desarrollo (ANID) under grant numbers Anillo ATE220045 and Fondecyt 1240411. Felipe Carreño-López extends his gratitude to Universidad de los Andes (Chile) for the support provided through the Concurso de Formación de Capital Humano–FAI Postdoctorado 2024 (No. 000100187153) and to ANID for the funding received through the Fondecyt de Postdoctorado 2025 (No. 3250412).

Appendix A. Supplementary data

Supplementary material related to this article can be found online at https://doi.org/10.1016/j.bej.2025.110049.

Data availability

I have shared the link to my data as Research Data

Data (Original data) (GitHub)

References

[1] J. van Groenestijn, N. Kraakman, Recent developments in biological waste gas purification in europe, Chem. Eng. J. 113 (2) (2005) 85–91, http://dx.doi.org/10.1016/j.cej.2005.03.007, Selected papers from the USC-CSC-TRG Biofiltration Conference, October 2004. URL https://www.sciencedirect.com/science/article/pii/S1385894705001063.

[2] V. Senatore, T. Zarra, M.G. Galang, G. Oliva, A. Buonerba, C.-W. Li, V. Belgiorno, V. Naddeo, Full-scale odor abatement technologies in wastewater treatment plants (WWTPs): A review, Water 13 (24) (2021) http://dx.doi.org/10.3390/w13243503, URL https://www.mdpi.com/2073-4441/13/24/3503.

[3] R. Muñoz, L. Meier, I. Diaz, D. Jeison, A review on the state-of-the-art of physical/chemical and biological technologies for biogas upgrading, Rev. Environ. Sci. Bio/Technology 14 (2015) 727–759, http://dx.doi.org/10.1007/s11157-015-9379-1.

[4] R. Lebrero, J.M. Estrada, R. Muñoz, G. Quijano, Toluene mass transfer characterization in a biotrickling filter, Biochem. Eng. J. 60 (2012) 44–49, http://dx.doi.org/10.1016/j.bej.2011.09.017, URL https://www.sciencedirect.com/science/article/pii/S1369703X11002622.

[5] H. Wu, H. Yan, Y. Quan, H. Zhao, N. Jiang, C. Yin, Recent progress and perspectives in biotrickling filters for VOCs and odorous gases treatment, J. Environ. Manag. 222 (2018) 409–419, http://dx.doi.org/10.1016/j.jenvman.2018.06.001, URL https://www.sciencedirect.com/science/article/pii/S0301479718306418.

[6] Y. Cheng, H. He, C. Yang, G. Zeng, X. Li, H. Chen, G. Yu, Challenges and solutions for biofiltration of hydrophobic volatile organic compounds, Biotech. Adv. 34 (6) (2016) 1091–1102, http://dx.doi.org/10.1016/j.biotechadv.2016.06.007, URL https://www.sciencedirect.com/science/article/pii/S0734975016300751.

[7] H.H.J. Cox, M.A. Deshusses, Biotrickling filters, in: Bioreactors for Waste Gas Treatment, Springer Netherlands, Dordrecht, 2001, pp. 99–131, http://dx.doi.org/10.1007/978-94-017-0930-9_4.

[8] G. Cabrera, F. Almenglo, M. Ramírez, D. Cantero, 2.30 - Biofilters, in: M. Moo-Young (Ed.), Comprehensive Biotechnology (Third Edition), third ed., Pergamon, Oxford, 2019, pp. 428–445, http://dx.doi.org/10.1016/B978-0-444-64046-8.00082-3, URL https://www.sciencedirect.com/science/article/pii/B9780444640468000823.

[9] C.R. Cattaneo, R. Muñoz, G.V. Korshin, V. Naddeo, V. Belgiorno, T. Zarra, Biological desulfurization of biogas: A comprehensive review on sulfide microbial metabolism and treatment biotechnologies, Sci. Total Environ. 893 (2023) 164689, http://dx.doi.org/10.1016/j.scitotenv.2023.164689, URL https://www.sciencedirect.com/science/article/pii/S0048969723033120.

[10] S. Liu, P.-F. Gao, S. Li, H. Fu, L. Wang, Y. Dai, M. Fu, A review of the recent progress in biotrickling filters: packing materials, gases, micro-organisms, and CFD, Environ. Sci. Pollut. Res. (2023) http://dx.doi.org/10.1007/s11356-023-31004-7.

[11] M. Hernández, G. Quijano, R. Muñoz, S. Bordel, Modeling of VOC mass transfer in two-liquid phase stirred tank, biotrickling filter and airlift reactors, Chem. Eng. J. 172 (2) (2011) 961–969, http://dx.doi.org/10.1016/j.cej.2011.07.008, URL https://www.sciencedirect.com/science/article/pii/S1385894711008357.

[12] S. Kim, M.A. Deshusses, Determination of mass transfer coefficients for packing materials used in biofilters and biotrickling filters for air pollution control. 1. Experimental results, Chem. Eng. Sci. 63 (4) (2008) 841–855, http://dx.doi.org/10.1016/j.ces.2007.10.011, URL https://www.sciencedirect.com/science/article/pii/S0009250907007968.

[13] R.M.M. Diks, S.P.P. Ottengraf, Verification studies of a simplified model for the removal of dichloromethane from waste gases using a biological trickling filter, Bioprocess Eng. 6 (3) (1991) 93–99, http://dx.doi.org/10.1007/BF00369061.

[14] S. Hartmans, J. Tramper, Dichloromethane removal from waste gases with a trickle-bed bioreactor., Bioprocess Eng. 6 (1991) 83–92, http://dx.doi.org/10.1007/bf00369060.

[15] C. Yang, G. Yu, G. Zeng, H. Yang, F. Chen, C. Jin, Performance of biotrickling filters packed with structured or cubic polyurethane sponges for VOC removal, J. Environ. Sci. 23 (8) (2011) 1325–1333, http://dx.doi.org/10.1016/S1001-0742(10)60565-7, URL https://www.sciencedirect.com/science/article/pii/S1001074210605657.

[16] F. Caicedo, J.M. Estrada, J.P. Silva, R. Muñoz, R. Lebrero, Effect of packing material configuration and liquid recirculation rate on the performance of a biotrickling filter treating VOCs, J. Chem. Technol. Biotechnol. 93 (8) (2018) 2299–2306, http://dx.doi.org/10.1002/jctb.5573, URL https://onlinelibrary.wiley.com/doi/abs/10.1002/jctb.5573.

[17] T.L. Dupnock, M.A. Deshusses, Development and validation of a comprehensive model for biotrickling filters upgrading biogas, Chem. Eng. J. 407 (2021) 126614, http://dx.doi.org/10.1016/j.cej.2020.126614, URL https://www.sciencedirect.com/science/article/pii/S138589472032742X.

[18] F. Carreño-López, P.A. Moreno-Casas, F. Scott, J. Iza, J. Sierra-Pallares, R. Muñoz, A. Vergara-Fernández, A convenient method to validate the gas flow of a CFD-CT simulation applied on a packed bed used in gas biofiltration through residence time distributions, Chem. Eng. J. 451 (2023) 138795, http://dx.doi.org/10.1016/j.cej.2022.138795, URL https://www.sciencedirect.com/science/article/pii/S1385894722042760.

[19] M.J. Lorences, J.-P. Laviolette, G.S. Patience, M. Alonso, F.V. Díez, Fluid bed gas RTD: Effect of fines and internals, Powder Technol. 168 (1) (2006) 1–9, http://dx.doi.org/10.1016/j.powtec.2006.06.010, URL https://www.sciencedirect.com/science/article/pii/S0032591006002361.

[20] A. Vergara-Fernández, S. Revah, P. Moreno-Casas, F. Scott, Biofiltration of volatile organic compounds using fungi and its conceptual and mathematical modeling, Biotech. Adv. 36 (4) (2018) 1079–1093, http://dx.doi.org/10.1016/j.biotechadv.2018.03.008, URL https://www.sciencedirect.com/science/article/pii/S0734975018300466.

[21] S. Sharvelle, E. McLamore, M.K. Banks, Hydrodynamic characteristics in Biotrickling filters as affected by packing material and hydraulic loading rate, J. Environ. Eng. 134 (5) (2008) 346–352, http://dx.doi.org/10.1061/(ASCE)0733-9372(2008)134:5(346).

[22] G. Trejo-Aguilar, S. Revah, R. Lobo-Oehmichen, Hydrodynamic characterization of a trickle bed air biofilter, Chem. Eng. J. 113 (2) (2005) 145–152, http://dx.doi.org/10.1016/j.cej.2005.04.001, Selected papers from the USC-CSC-TRG Biofiltration Conference, October 2004. URL https://www.sciencedirect.com/science/article/pii/S1385894705001324.

[23] L. Prades, A. Dorado, J. Climent, X. Guimerà, S. Chiva, X. Gamisans, CFD modeling of a fixed-bed biofilm reactor coupling hydrodynamics and biokinetics, Chem. Eng. J. 313 (2017) 680–692, http://dx.doi.org/10.1016/j.cej.2016.12.107, URL https://www.sciencedirect.com/science/article/pii/S1385894716318782.

[24] A.M. Montebello, M. Baeza, J. Lafuente, D. Gabriel, Monitoring and performance of a desulphurizing biotrickling filter with an integrated continuous gas/liquid flow analyser, Chem. Eng. J. 165 (2) (2010) 500–507, http://dx.doi.org/10.1016/j.cej.2010.09.053, URL https://www.sciencedirect.com/science/article/pii/S1385894710008831.

[25] F.X. Prenafeta-Boldú, J. Illa, J.W. van Groenestijn, X. Flotats, Influence of synthetic packing materials on the gas dispersion and biodegradation kinetics in fungal air biofilters, Appl. Microbiol. Biotechnol. 79 (2) (2008) 319–327, http://dx.doi.org/10.1007/s00253-008-1433-2.

[26] L.A. Panes-Ruiz, L. Riemenschneider, M.M. Al Chawa, M. Löffler, B. Rellinghaus, R. Tetzlaff, V. Bezugly, B. Ibarlucea, G. Cuniberti, Selective and self-validating breath-level detection of hydrogen sulfide in humid air by gold nanoparticle-functionalized nanotube arrays, Nano Res. 15 (3) (2022) 2512–2521, http://dx.doi.org/10.1007/s12274-021-3771-7.

[27] Y. Andres, E. Dumont, P.L. Cloirec, E. Ramirez-Lopez, Wood bark as packing material in a biofilter used for air treatment, Environ. Technol. 27 (12) (2006) 1297–1301, http://dx.doi.org/10.1080/09593332708618747, PMID: 17285934.

[28] J.G. Monroy, J. González-Jiménez, J.L. Blanco, Overcoming the slow recovery of MOX gas sensors through a system modeling approach, Sensors 12 (10) (2012) 13664–13680, http://dx.doi.org/10.3390/s121013664, URL https://www.mdpi.com/1424-8220/12/10/13664.

[29] H.S. Fogler, Elements of Chemical Reaction Engineering, fourth ed., Prentice Hall, 2005.

[30] O. Levenspiel, Tracer technology: Modeling the flow of fluids, in: Fluid Mechanics and Its Applications, vol. 96, Springer, New York, NY, 2012, http://dx.doi.org/10.1007/978-1-4419-8074-8.

[31] J.R. Ferreira, A.P. Senna, E.N. Macêdo, D.C. Estumano, Aerobic bioreactors: A Bayesian point of view applied to hydrodynamic characterization and experimental evaluation of tracers, Chem. Eng. Sci. 277 (2023) 118850, http://dx.doi.org/10.1016/j.ces.2023.118850, URL https://www.sciencedirect.com/science/article/pii/S0009250923004062.

[32] B. Efron, R.J. Tibshirani, An Introduction to the Bootstrap, Chapman and Hall/CRC, New York, 1994, http://dx.doi.org/10.1201/9780429246593.

[33] J.B. Rawlings, J.G. Ekerdt, Chemical Reactor Analysis and Design Fundamentals, Nob Hill Publishing, Madison, WI, 2001, http://dx.doi.org/10.5281/zenodo.1257893.

[34] A. Bonilla-Petriciolet, I. Rodríguez-Donis, Uncertainty analysis in chemical engineering models, Chem. Eng. Trans. 74 (2019) 1213–1218, http://dx.doi.org/10.3303/CET1974203.

[35] K. Abdi, K.B. McAuley, Parameter estimation and prediction uncertainties for multi-response kinetic models with uncertain inputs, AIChE J. 69 (6) (2023) e18058, http://dx.doi.org/10.1002/aic.18058.

[36] F. Rossi, R. Singh, C.C. Pantelides, Present and future of model uncertainty quantification in process systems engineering, Chem. Eng. Trans. 76 (2019) 139–144, http://dx.doi.org/10.3303/CET1976024.

[37] N.P. Kazmierczak, Bootstrap methods for quantifying the uncertainty of thermodynamic parameters, Anal. Chim. Acta 1202 (2022) 339664, http://dx.doi.org/10.1016/j.aca.2022.339664.

[38] M. Newville, T. Stensitzki, D.B. Allen, A. Ingargiola, LMFIT: Non-Linear Least-Squares Minimization and Curve-Fitting for Python, Zenodo, 2014, http://dx.doi.org/10.5281/zenodo.11813, URL https://lmfit.github.io/lmfit-py/.

[39] P.A. Moreno-Casas, F. Scott, J. Delpiano, J.A. Abell, F. Caicedo, R. Muñoz, A. Vergara-Fernández, Mechanistic description of convective gas–Liquid mass transfer in Biotrickling filters using CFD modeling, Environ. Sci. Technol. 54 (1) (2020) 419–426, http://dx.doi.org/10.1021/acs.est.9b02662, PMID: 31789508.

[40] S. Gunashekar, K.M. Pillai, B.C. Church, N.H. Abu-Zahra, Liquid flow in polyurethane foams for filtration applications: a study on their characterization and permeability estimation, J. Porous Mater. 22 (3) (2015) 749–759, http://dx.doi.org/10.1007/s10934-015-9948-2.

[41] M.I. Jaramillo-Gutiérrez, J.A. Pedraza-Avella, I. González, E.P. Rivero, M.R. Cruz-Díaz, Design equations based on micro/macromixing theoretical analysis of rtd curves for a tubular concentric electrochemical reactor with expanded meshes as electrodes, Rev. Mex. de Ingeniería Química 21 (1) (2022) http://dx.doi.org/10.24275/rmiq/Cat2434, Artículo recibido: 18 de abril de 2021; aceptado: 7 de diciembre de 2021. URL https://rmiq.org/iqfvp/Numbers/V21/No1/Cat2434.pdf.

[42] M.R. Cruz-Díaz, A. Laureano, F.A. Rodríguez, L.F. Arenas, J. J. H. Pijpers, E.P. Rivero, Modelling of flow distribution within spacer-filled channels fed by dividing manifolds as found in stacks for membrane-based technologies, Chem. Eng. J. 423 (2021) 130232, http://dx.doi.org/10.1016/j.cej.2021.130232, URL https://www.sciencedirect.com/science/article/pii/S1385894721018209.

[43] S. Petrazzuoli, A. Pironti, F. Santarelli, Flow and dispersion in small-diameter packed beds: Particle-resolved CFD modeling of wall effects and preferential pathways, Chem. Eng. Sci. 230 (2021) 116208.

[44] P. Lovreglio, K.A. Buist, J.A.M. Kuipers, E.A.J.F. Peters, Analysis of particle-resolved CFD results for dispersion in packed beds, Fluids 7 (6) (2022) http://dx.doi.org/10.3390/fluids7060199, URL https://www.mdpi.com/2311-5521/7/6/199.